RSC Applied Polymers

PAPER

View Article Online
View Journal | View Issue

Cite this: *RSC Appl. Polym.*, 2025, **3**, 1495

Multicomponent tandem polymerization for the preparation of a pyrazole-containing porous organic polymer for iodine capture and the nitro reduction reaction

Xulin Liang, Bingyan Zhou, Qixiang Ma, Shengyu Feng, Dengxu Wang * and Hongzhi Liu

Developing a straightforward and efficient strategy for incorporating functionality in porous materials is of paramount importance. Functionality can endow these materials with enhanced performance in established applications or enable new performances in emerging application domains. Herein, we present the synthesis of a pyrazole-containing porous organic polymer (**PPOP**) *via* a multicomponent tandem polymerization reaction involving tetrakis(4-ethynylphenyl)silane, terephthaloyl chloride, and hydrazine hydrate. The integration of pyrazole units into a porous network bestows new functionality on **PPOP** and leads to excellent iodine capture performance and suitable support for silver nanoparticles, which can act as an efficient catalyst for nitro reduction reactions. **PPOP** exhibits an iodine vapor adsorption capacity of 3.52 ± 0.15 g g^{-1}, which is comparable to or higher than many existing iodine adsorbents. Mechanistic investigations reveal that the adsorption is governed by a combination of physisorption and chemisorption. Chemisorption is facilitated by electron transfer from electron-rich moieties, particularly pyrazole groups, within the adsorbent to I_2, leading to the formation of polyiodides and charge-transfer complexes. When loaded with silver nanoparticles, **PPOP** can catalyze the reduction reactions of nitroaromatics to aminoaromatics with nearly complete conversion within 20 min at room temperature. This research underscores the utility of multicomponent tandem polymerization reactions for the rational design and synthesis of functional POPs with potential applications in diverse fields.

Received 10th May 2025,
Accepted 18th August 2025

DOI: 10.1039/d5lp00135h

rsc.li/rscapplpolym

1 Introduction

Porous organic polymers (POPs) are a class of materials with micro- or mesoporous structures characterized by high porosity, large specific surface areas, and exceptional chemical and thermal stability.[1–4] POPs have garnered significant attention in various applications, including gas storage and separation, iodine adsorption, energy storage and conversion, and catalysis.[5–11] Functionality plays a pivotal role in optimizing the performance of POPs for targeted applications. Generally, the functionalities of POPs can be realized through two primary approaches: the selection of functional monomers[12–14] and post-synthetic modification of the existing materials.[15,16] However, the synthesis of many functional monomers is often intricate, and in some cases, it fails to construct POPs due to the poor tolerance of functional groups in many reactions. Post-modification, on the other hand, may lead to the collapse of porous networks, and its efficiency is relatively low because of the inherent limitations of heterogeneous reactions.[17] Therefore, there is an urgent need to develop a straightforward and efficient methodology for constructing functional POPs.

Multicomponent tandem polymerizations (MCTPs) are a powerful synthetic strategy that integrates multiple reaction steps into a single-pot process. This approach effectively eliminates the need for intermediate isolation and purification,[18] significantly enhancing synthetic efficiency. Moreover, MCTPs enable the construction of complex polymer architectures that are difficult to achieve using traditional stepwise polymerization methods.[19] To date, MCTPs have been successfully applied to the synthesis of linear polymers, yielding well-defined structures with tailored properties.[18,20,21] Nevertheless, the exploration of this strategy for the construction of POPs remains limited.[13,22–25] Given the wide variety of monomers and synthetic strategies available in MCTPs, we hypothesize that one-pot multicomponent tandem

National Engineering Research Center for Colloidal Materials & Key Laboratory of Special Functional Aggregated Materials, Ministry of Education, Shandong Key Laboratory of Advanced Organosilicon Materials and Technologies, School of Chemistry and Chemical Engineering, Shandong University, Jinan 250100, P. R. China. E-mail: dxwang@sdu.edu.cn

polymerization could be a highly effective method for fabricating amorphous POPs, allowing precise control of functionality.

In this study, we report a novel three-component tandem polymerization involving tetrakis(4-ethynylphenyl)silane, terephthaloyl chloride, and hydrazine hydrate. Under mild conditions, this reaction affords a pyrazole-containing porous organic polymer (**PPOP**) in high yield (Scheme 1a). The incorporation of pyrazole units into the porous network imparts new functionalities. The resulting **PPOP** was employed as an efficient adsorbent for capturing iodine in both vapor and solution phases and as a support for loading silver nanoparticles (PPOP-Ag), resulting in a catalyst capable of reducing nitroaromatics to aminoaromatics.

2 Experimental

2.1 Materials

Tetrakis(4-ethynylphenyl)silane was prepared according to the method described in the literature.[26] All commercially available chemicals and reagents were sourced from Energy Chemicals and used directly without further purification.

2.2 Synthesis of the pyrazole-containing porous organic polymer (PPOP)

Under argon, tetrakis(4-ethynylphenyl)silane (432 mg, 1 mmol), terephthaloyl dichloride (410 mg, 2 mmol), CuI (30 mg, 0.16 mmol), bis(triphenylphosphine) palladium dichloride (60 mg, 0.08 mmol), triethylamine (560 μL, 2 mmol), and tetrahydrofuran (70 mL) were sequentially added into a 100 mL three-necked flask. The reaction mixture was stirred at 50 °C for 36 h. Subsequently, *N*, *N*-dimethylformamide (20 mL) and hydrazine hydrate (363 μL, 6 mmol) were added, and the resulting mixture was stirred at 60 °C for 48 h. The mixture was then allowed to cool to room temperature, followed by the addition of hexane (400 mL). The mixture was filtered, and the precipitate was sequentially washed with water, methanol, tetrahydrofuran, acetone, and chloroform. The crude product was further purified using Soxhlet extraction with tetrahydrofuran for 24 h and methanol for 24 h. Finally, the product was dried in a vacuum oven at 75 °C for 48 h, yielding a tawny solid (0.60 g). Yield: 80%. Elemental analysis calculated (%) for $C_{48}H_{32}N_8Si$: C: 76.98, H: 4.31, N: 14.96; found: C: 70.5, H: 4.17, N: 7.00.

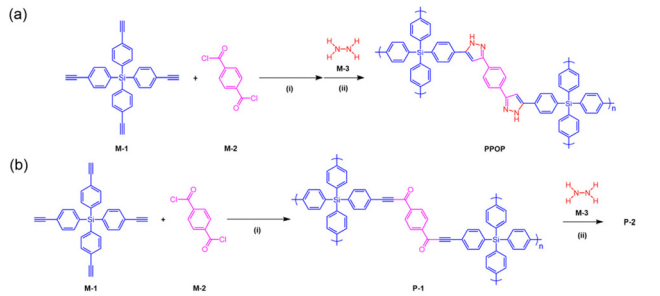

Scheme 1 Synthetic routes of the pyrazole-based porous organic polymers, **PPOP** (a) by multicomponent tandem polymerization and **P-2** by the post-modification reaction of the intermediate product, **P-1** (b). Reaction conditions: (i) $Pd(PPh_3)_2Cl_2$, CuI, THF, Et_3N, 50 °C, 36 h; (ii) DMF, 60 °C, 48 h.

2.3 Synthesis of comparative porous organic polymers, P-1 and P-2

2.3.1 P-1. The preparation process and post-processing of **P-1** were similar to those of **PPOP**, with the exception that the reaction was terminated after the first step. The resulting product was afforded as a tawny solid (0.58 g). Yield: 83%. Elemental analysis calculated (%) for $C_{48}H_{24}O_4Si$: C: 83.22, H: 3.49; found: C: 50.80, H: 2.71.

2.3.2 P-2. The preparation process and post-processing of **P-2** were similar to those of **PPOP**, with the exception that the intermediate product **P-1** from the first step was isolated and purified prior to utilization in the subsequent reaction. The product was afforded as a tawny solid (0.58 g). Yield: 72%. Elemental analysis calculated (%) for $C_{48}H_{32}N_8Si$: C: 76.98, H: 4.31, N: 14.96; found: C: 62.50, H: 4.33, N: 5.23.

2.4 Synthesis of Ag nanoparticle-loaded polymers

2.4.1 PPOP-Ag. 200 mg of **PPOP** was introduced into a 40 mL methanol solution containing 20 mg of $AgNO_3$, and the mixture was stirred at room temperature for 12 h. Subsequently, a freshly prepared $NaBH_4$ aqueous solution (0.05 M, 5.0 mL) was added, and the mixture was stirred for an additional 2 h. The solid product was then isolated *via* centrifugation, followed by washing with water, ethanol, and diethyl ether. Finally, the product was dried under vacuum for 24 h, yielding a fine black solid (0.19 g). Yield: 95%. Ag: 3.08 wt%.

2.4.2 P-1-Ag. The preparation process and post-processing of P-1-Ag were similar to those of PPOP-Ag, except that the **PPOP** was changed into **P-1**. The resulting product was afforded as a fine black solid (0.19 g). Yield: 95%. Ag: 3.56 wt%.

2.5 Iodine capture by PPOP, P-1, and P-2

The efficiency of **PPOP** in capturing iodine was evaluated using two methods: vapor-phase adsorption and solution-phase adsorption, whereas **P-1** and **P-2** were evaluated exclusively *via* vapor-phase adsorption. All iodine used in these experiments was nonradioactive.

2.5.1 Iodine adsorption in vapor. The experiments were conducted by placing 20 mg of the sample and an iodine pill into two interconnected, pre-weighed bottles. The system was degassed under vacuum and maintained at 75 °C. Iodine uptake was measured at various time intervals.

2.5.2 Iodine adsorption in solutions. The experiments involved suspending **PPOP** in *n*-hexane (1 mg mL^{-1}) at room temperature. After iodine adsorption by the material, the remaining iodine concentrations were measured using a UV-vis spectrophotometer. The effect of initial iodine concentrations was investigated by introducing iodine solutions with

concentrations ranging from 100 to 2000 ppm (100, 200, 400, 600, 800, 1000, 1200, 1400, 1600, 1800, and 2000 ppm) in the presence of **PPOP** (1 mg mL^{-1}) and allowing the system to equilibrate for 36 h. The effect of contact time was evaluated by suspending **PPOP** (1 mg mL^{-1}) in an iodine solution (1000 ppm) and measuring the iodine concentrations at intervals of 30 min, 1 h, 2 h, 4 h, 8 h, 12 h, 24 h, 36 h, and 48 h.

The removal efficiency (q, %) and adsorption capacity (Q_e, g g^{-1}) were calculated using eqn (1) and (2).

$$q = \frac{C_0 - C_e}{C_0} \times 100\% \quad (1)$$

$$Q_e = \frac{C_0 - C_e}{m} \times V \quad (2)$$

where C_0 (g L^{-1}) and C_e (g L^{-1}) represent the initial and equilibrium iodine concentrations, respectively, V (L) is the solution volume, and m (g) is the mass of **PPOP**.

2.6 Adsorption equilibrium and kinetics

The adsorption kinetics were investigated using pseudo-first-order and pseudo-second-order models, which are expressed by eqn (3) and (4), respectively.

$$\ln(Q_e - Q_t) = \ln Q_e - K_1 t \quad (3)$$

$$\frac{t}{Q_t} = \frac{t}{Q_e} + \frac{1}{K_2 (Q_e)^2} \quad (4)$$

where Q_t (g g^{-1}) and Q_e (g g^{-1}) represent the amounts of iodine adsorbed per gram of **PPOP** at time t and at equilibrium, respectively. K_1 (min^{-1}) and K_2 (g g^{-1} min^{-1}) are the rate constants of the pseudo-first-order model and pseudo-second-order models, respectively.

The adsorption process was further analysed using the Langmuir and Freundlich isotherms, which are expressed by eqn (5) and (6).

$$\frac{C_e}{Q_e} = \frac{C_e}{Q_m} + \frac{1}{K_L Q_m} \quad (5)$$

$$\ln Q_e = \ln K_F + \frac{1}{n} \times \ln C_e \quad (6)$$

where Q_m (g g^{-1}) and C_e (g L^{-1}) are the maximum extent of adsorption and the iodine concentration at equilibrium. K_L (L g^{-1}) and K_F (L g^{-1}) are constants, and n is a constant indicative of the adsorption intensity.

2.7 Reusability of PPOP for iodine capture in vapor

PPOP (20 mg) and an iodine pill (300 mg) were placed in two interconnected, sealed, and pre-weighed vials. The system was degassed under vacuum and then maintained at 75 °C in an oven for 24 h to measure the iodine adsorption by weight. After adsorption, the iodine-loaded samples were soaked in ethanol or *n*-hexane for 2 h, followed by centrifugation to remove the supernatant. This washing process was repeated several times until no further colour change was observed in the solutions. Subsequently, the washed samples were dried and reused for iodine adsorption under the same conditions. This recycled process was repeated five times.

2.8 Nitro reduction reaction catalysed by Ag nanoparticle-loaded porous organic polymers

2.8.1 Typical model reaction for the reduction of 4-nitrophenol by Ag nanoparticle-loaded polymers. A 100 mL flask equipped with a magnetic stirring bar was charged with 4-nitrophenol (4-NP, 13.9 mg, 0.1 mmol), deionized water (45 mL), and catalyst (10 mg). The mixture was stirred for 20 min, after which a freshly prepared $NaBH_4$ aqueous solution (200 mM, 5.0 mL) was added. The resulting mixture was monitored using UV-vis spectrophotometry, with measurements taken across the wavelength range of 250 nm to 500 nm.

Given that excess $NaBH_4$ was employed, the reaction was assumed to follow pseudo-first-order kinetics. The apparent rate constant (K_{app}, s^{-1}) and the normalized rate constant (K', g^{-1} s^{-1}) were calculated using eqn (7) and (8), respectively.

$$\ln\left(\frac{C_t}{C_0}\right) = \ln\left(\frac{A_t}{A_0}\right) = -K_{app} \cdot t \quad (7)$$

$$K' = \frac{K_{app}}{m} \quad (8)$$

where C_0 and C_t (g L^{-1}) indicate the initial and instantaneous concentrations of 4-NP, while A_0 and A_t denote their corresponding absorbance values. m (g) is the mass of PPOP-Ag used in this reaction.

2.8.2 General method for the reduction of nitroaromatics by PPOP-Ag. A 100 mL flask equipped with a magnetic stirring bar was charged with nitroaromatics (NAs) (0.1 mmol), deionized water (45 mL), and PPOP-Ag (10 mg). The mixture was stirred for 20 min, after which a freshly prepared $NaBH_4$ aqueous solution (200 mM, 5.0 mL) was added. The resulting mixture was monitored using UV-vis spectrophotometry, with measurements taken across the wavelength range of 250 nm to 500 nm, except that the range was adjusted to 220 nm to 500 nm for 4-chloronitrobenzene. Following the completion of the reaction, the catalysts were recovered *via* filtration and sequentially washed with ethanol and diethyl ether. The reaction mixture was extracted with ethyl acetate. After drying the organic layer over anhydrous Na_2SO_4, the solvent was evaporated under reduced pressure. The resulting crude product was purified by column chromatography. The isolated yield was calculated after drying under high vacuum. The structure was confirmed by ^1H NMR spectroscopy.

2.8.3 Reusability of PPOP-Ag and P-1-Ag for nitro reduction. The reusability of catalysts was evaluated by the reduction of 4-NP to 4-aminophenol. As detailed in Section 2.8.2, upon the completion of the reaction, the catalysts were recovered *via* filtration. Subsequently, they were washed with ethanol and diethyl ether, then dried and redeployed for the subsequent nitro reduction under the same conditions. This recycled process was repeated five times.

3 Results and discussion

3.1 Synthesis and characterization

As depicted in Scheme 1a, the pyrazole-containing porous organic polymer (**PPOP**) was synthesized *via* a one-pot procedure, a three-component tandem polymerization of tetrakis (4-ethynylphenyl)silane (**M-1**), terephthalic dichloride (**M-2**), and hydrazine hydrate (**M-3**). This synthetic approach effectively integrates Sonogashira coupling and Michael addition–cyclocondensation reactions, demonstrating high efficiency in the preparation of linear polymers with high molecular weight.[20] The resulting material exhibits insolubility in various solvents such as water, ethanol, tetrahydrofuran, methanol, chloroform, and DMF. In addition, to validate the advantage of the tandem multicomponent reaction, the intermediate product, **P-1**, was synthesized *via* the Sonogashira reaction of **M-1** and **M-2** and subsequently isolated. **P-1** was then post-functionalized with **M-3**, yielding a structurally analogous polymer, **P-2** (Scheme 1b).

To confirm the successful binding of the three components, **PPOP** was comprehensively characterized using FT-IR spectroscopy, solid-state ^{13}C CP/MAS NMR, and elemental analysis. As shown in Fig. 1a and S1a–b, the C≡C–H stretching vibration in **M-1** and the C═O stretching vibration in **M-2** were observed at 3280 cm^{-1} and 1728 cm^{-1}. **M-3** exhibits H–N–H stretching vibrations at 3325 cm^{-1} and 3193 cm^{-1} (Fig. 1a and S1c). **P-1** exhibits a characteristic C═O stretching vibration at 1714 cm^{-1} and a new C≡C–C stretching vibration at 2194 cm^{-1}, confirming the successful reaction between **M-1** and **M-2** (Fig. 1a and S1e). In comparison, the infrared spectrum of **PPOP** shows the disappearance of the C≡C–C and C═O peaks and the emergence of new peaks at 3346 cm^{-1} (N–H) and 1614 cm^{-1} (C═N), confirming the integration of three units into the framework and the formation of the pyrazole structure (Fig. S1d). In the ^{13}C NMR spectra, the carbon atoms from *C*≡*C*–H in **M-1** are observed at 77.6 and 82.3 ppm, while the carbon atom from the *C*═O group in **M-2** (Fig. 1b and S2a–b) is observed at 167.5 ppm. After the tandem polymerization, **PPOP** exhibited a new peak at 150.1 ppm, attributable to the carbon atom from C═N, in comparison with the peaks at 176.5 ppm (C═O) and at 88.0 and 95.0 ppm (*C*≡*C*–C) in the intermediate **P-1** (Fig. 1b and S2c–d). **PPOP** exhibits a broad UV absorption extending into the visible region (λ > 500 nm), indicating its conjugated structure (Fig. S3). The XPS spectra show binding energy peaks for N 1s centred at 399.09 and 400.45 eV (Fig. S4), consistent with the presence of C═N and C–NH groups.[27,28] These findings verify the successful conversion of the ynone groups into the pyrazole ring system, as depicted in the proposed idealized repeating unit structure presented in Scheme 1.

The elemental analysis showed that the experimental nitrogen content (%) in **PPOP** deviates significantly (>50%) compared to the theoretical N composition. The discrepancy observed between the experimentally measured nitrogen content and the theoretical value is mainly attributed to the presence of silicon within the polymer backbone. In elemental analysis, the maximum decomposition temperature typically reaches only about 1150 °C. This temperature is inadequate for the complete decomposition of thermally stable silicon-based compounds such as silicon carbide, silicon nitride, and silicon dioxide. These compounds can form during pyrolysis as a consequence of interactions between silicon and carbon, nitrogen, or oxygen, resulting in an underestimation of the nitrogen content. To verify the reproducibility of the result and eliminate potential measurement errors, a second independent elemental analysis was conducted on the same batch of **PPOP**. The nitrogen content was once again found to be approximately 6.9 wt%, consistent with the initial result. This further substantiates the conclusion that the deviation is caused by silicon interference, impeding accurate quantification. These results reveal that the tandem polymerization has successfully occurred and that the pyrazole linkages have been effectively incorporated into the porous network of **PPOP**.

Additionally, the structure of comparable polymer **P-2** was determined by FT-IR and elemental analysis. The peaks at 3302 cm^{-1} (N–H) and 1602 cm^{-1} (C═N) were detected in **P-2**, whereas the C═C and C═O peaks characteristic of **P-1** were absent, confirming pyrazole group formation *via* the reaction with **M-3** (Fig. S1f) and consistent with that of **P-1**. However, elemental analysis revealed that **P-2** contained 5.23 wt% nitrogen, which is notably lower than that of **PPOP** (7.00 wt%), suggesting that the tandem polymerization pathway offers a more efficient conversion of functional groups into nitrogen-containing moieties.

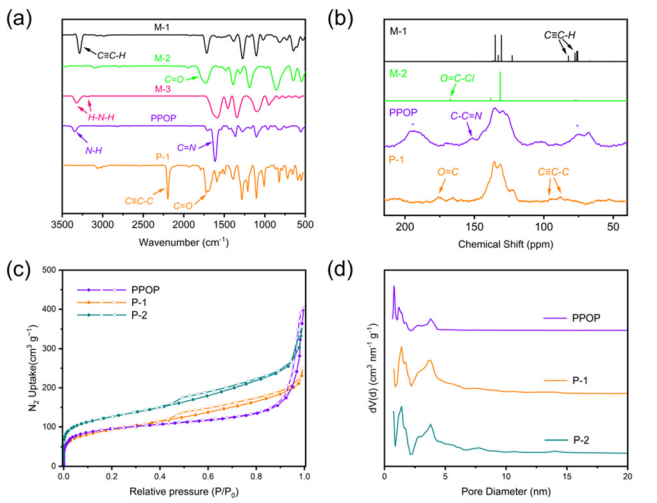

Fig. 1 (a) FT-IR spectroscopy of **M-1** to **M-3**, **PPOP**, and **P-1**; (b) ^{13}C NMR spectra of **M-1** to **M-2** in solutions, and **PPOP** and **P-1** in the solid state; (c) nitrogen adsorption and desorption isotherm of **PPOP**, **P-1**, and **P-2**; and (d) pore size distribution curve of **PPOP**, **P-1** and **P-2**. Asterisks denote the spinning sidebands.

3.2 Stability and morphology

The thermal stability of **PPOP** was evaluated using thermogravimetric analysis (TGA). The results indicate that **PPOP** exhibits excellent thermal stability with T_d (5% mass loss) at

approximately 320 °C (Fig. S5). To evaluate the stability of **PPOP** under harsh conditions, **PPOP** specimens were exposed to 1 M NaOH, 1 M HCl, and DMF for a duration of 24 h, subsequently washed with tetrahydrofuran, and dried at 75 °C in a vacuum oven for 24 h. FT-IR spectroscopy was then performed on the treated samples (Fig. S6). The results revealed that all the characteristic absorption bands of the pristine **PPOP** were preserved following the treatments. This observation suggests that **PPOP** maintains its structural integrity and exhibits good chemical stability when exposed to harsh environments. As expected, **PPOP** was found to be amorphous, lacking the long-range crystallographic order, evidenced by X-ray diffraction (XRD) analysis (Fig. S7). The morphology of **PPOP** was examined using field-emission scanning electron microscopy (FE-SEM). The image reveals that the polymer consists of nanostructured irregular shapes with a consistent size distribution, averaging approximately 50 nm (Fig. S8).

3.3 Porosity

The porous property and porous structure of polymers were evaluated using the nitrogen adsorption–desorption isotherm at 77 K (Fig. 1c and Table 1). The N_2 isotherms of **PPOP**, **P-1**, and **P-2** exhibit a combination of type I and type IV behaviour, characterized by a sharp uptake at low relative pressures, followed by a gradual increase in adsorption at higher relative pressures accompanied by a hysteresis loop. This pattern indicates the coexistence of micropores and mesopores within the framework of polymers. The Brunauer–Emmett–Teller (BET) specific surface area (S_{BET}) and the total pore volume (V_{total}) of **PPOP** are 379 ± 20 $m^2\ g^{-1}$ and 0.65 ± 0.01 $cm^3\ g^{-1}$, respectively. The micropore surface area (S_{micro}) and the micropore volume (V_{micro}) were calculated to be 279 $m^2\ g^{-1}$ and 0.12 $cm^3\ g^{-1}$, respectively, using the *t*-plot method. Consequently, the V_{micro}/V_{total} ratio of the network was 0.20, confirming the predominance of the mesoporous structure in **PPOP**. The nonlocal density functional theory was used to evaluate the pore size distribution, revealing the presence of uniform micropores with average diameters of 0.78 nm and 1.18 nm, as well as broader mesopores ranging from 2 to 4 nm (Fig. 1d).

The S_{BET} of **P-1** and **P-2** are 325 ± 20 and 450 ± 20 $m^2\ g^{-1}$, respectively. Although the S_{BET} of **P-2** is higher than that of **PPOP**, **PPOP** exhibits superior microporosity, as evidenced by its higher S_{micro}, V_{total}, V_{micro}, and V_{micro}/V_{total} ratio. These metrics collectively indicate a more well-developed microporous structure in **PPOP** (Table 1, Fig. 1c and d). In terms of pore size distribution, both **P-1** and **P-2** exhibit a distinct peak centred at 1.41 nm, with an area approximately the same as the 1.18 nm peak observed in **PPOP**. Notably, the 0.78 nm micropore peak, which is evident in **PPOP**, is significantly diminished in **P-1** and **P-2**. Additionally, **P-1** and **P-2** exhibit a broader mesoporous region in the range of 2 to 6 nm, whereas **PPOP** shows a narrower mesopore distribution between 2 and 4 nm. These observations suggest that **PPOP** exhibits more well-developed microporous features and a tighter mesoporous structure compared to **P-1** and **P-2**. These findings indicate that the tandem polymerization strategy may yield materials with more favorable microporosity than those produced through post-synthetic modification.

3.4 Iodine capture of PPOP

PPOP, owing to the presence of pyrazole units within the structure, exhibits extensive potential applications. One significant application is its use as an adsorbent for the capture of iodine (I_2) because volatile radioactive iodine-containing species (^{129}I and ^{131}I) are considered a major form of nuclear waste and pose a threat to human health and environmental safety. Among various I_2 adsorbents, POPs offer distinct advantages, including exceptional surface area, chemical stability, and tunable skeletons.[29–32] In particular, the incorporation of nitrogen-rich units into POPs can enhance iodine capture by facilitating the formation of strong interactions through electron/charge transfer from these electron-rich units to electron-deficient iodine.[23,33–35] Consequently, the presence of pyrazole units in **PPOP** renders it a promising candidate for efficient I_2 adsorption.

3.4.1. Iodine capture in vapor. The I_2 capture was initially evaluated by exposing the sample to iodine vapor, with the adsorption capacity determined through gravimetric measurements. The samples and iodine vapor were placed in two interconnected, preweighed sealed vials. The system was degassed and maintained at 75 °C in an oven throughout the experiment. The mass of the sample was measured and recorded at regular time intervals until no further change in mass was observed. The results demonstrated that the I_2 capture was rapid within the first 5 h, followed by a gradual decrease in the

Table 1 Porosity data of polymers

Polymers	S_{BET}[a] ($m^2\ g^{-1}$)	S_{micro}[b] ($m^2\ g^{-1}$)	V_{total}[c] ($cm^3\ g^{-1}$)	V_{micro}[d] ($cm^3\ g^{-1}$)	V_{micro}/V_{total}
PPOP	379 ± 20	279	0.65 ± 0.01	0.12	0.20
P-1	325 ± 20	116	0.39 ± 0.01	0.058	0.15
P-2	450 ± 20	178	0.55 ± 0.01	0.078	0.14
Recycled **PPOP**[e]	82 ± 20	0	0.49 ± 0.01	0	0
PPOP-Ag	106 ± 20	61	0.16 ± 0.01	0.027	0.17
PPOP-Ag-1[f]	104 ± 20	61	0.14 ± 0.01	0.026	0.18

[a] Surface area calculated from the N_2 adsorption isotherm using the BET method. [b] Microporous surface area calculated from the N_2 adsorption isotherm using the *t*-plot method. [c] Total pore volume calculated at $P/P_0 = 0.99$. [d] Micropore volume derived using the *t*-plot method based on the de-Boer thickness equation. [e] The recycled **PPOP** sample after one cycle of iodine adsorption. [f] The recycled PPOP-Ag after one cycle of the nitro reduction reaction.

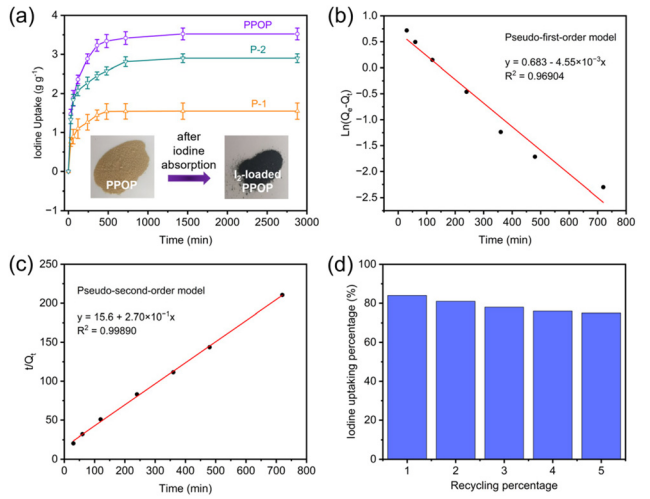

Fig. 2 (a) Gravimetric I_2 uptake of **PPOP**, **P-1**, and **P-2** as a function of time at 75 °C (inset: color changes of **PPOP** after absorbed iodine); (b) pseudo-first-order model spectra of **PPOP**; (c) pseudo-second-order model spectra of **PPOP**; and (d) recyclability of **PPOP** for iodine capture.

adsorption rate and eventual stabilization after approximately 10 h (Fig. 2a). The calculated iodine adsorption capacity was determined to be 3.52 ± 0.15 g g^{-1}. A distinct colour change from yellow to black upon iodine adsorption visually confirmed the adsorption process (inset in Fig. 2a). In addition, the UV-vis diffuse reflectance spectrum of I_2-loaded **PPOP** was measured (Fig. S3) and compared with that of pristine **PPOP** (Fig. S9). I_2-loaded **PPOP** exhibited continuous absorption over the full spectral range of 200–800 nm, consistent with the behavior of pristine **PPOP**. This result confirms that the conjugated framework remained intact after iodine loading. Notably, I_2-loaded **PPOP** exhibited a broader and red-shifted absorption band in the region of 300–450 nm, compared to the region of 300–350 nm observed in pristine **PPOP**. This finding indicates that the color of **PPOP** deepens upon I_2 loading, which aligns with the experimental observations (inset in Fig. 2a). The kinetic analysis demonstrated that the adsorption process well fits the pseudo-second-order model with the correlation coefficient value (R^2) of 0.99890, rather than the pseudo-first-order model with an R^2 of 0.96904 (Fig. 2b, c and Table 3).

To elucidate the role of pyrazole units and multicomponent tandem polymerization, the iodine vapor adsorption behaviours of **P-1** and **P-2** were also investigated. Similar to the adsorption behaviour of **PPOP**, both **P-1** and **P-2** exhibited rapid iodine uptake within the initial 4 h, after which the adsorption rate gradually declined (Fig. 2a). **P-1** reached a plateau at approximately 8 h, with an iodine uptake capacity of 1.55 ± 0.21 g g^{-1}, which is significantly lower than that of **PPOP**. **P-2** exhibited an adsorption trend similar to that of **PPOP**, attaining saturation around 10 h with a capacity of 2.90 ± 0.11 g g^{-1}, slightly lower than the performance of **PPOP**. These results underscore the crucial role of pyrazole units in iodine adsorption and demonstrate that the tandem polymerization strategy yields materials with superior iodine uptake efficiency compared to those synthesized *via* non-tandem routes.

The performance of **PPOP** is comparable to or higher than many iodine adsorbents, such as crystalline nitrone-linked covalent organic frameworks (COF) (3.0 g g^{-1}),[36] cage-based metal–organic frameworks (MOF) (1.561 g g^{-1}),[37] pyrazole-directed functionalization of activated collagen fibre (3.494 g g^{-1}),[38] nitrogen-rich POP (3.19 g g^{-1}),[39] three-dimensional hydrolysed collagen aerogel immobilized with catechin (2.227 g g^{-1}),[40] nitrogen-functionalized hyper-crosslinked polymers (HCPs) (2.83 g g^{-1}),[41] and hexaphenylbenzene-based conjugated microporous polymers (3.36 g g^{-1}).[42] The comparison results are summarized in Table 2.

However, **PPOP** underperforms when compared to certain high-performance porous organic polymers (POPs) reported in

Table 2 Comparison of the iodine uptakes of **PPOP** with other adsorbents

	Adsorbents	I_2 capacity in vapor[a] (g g^{-1})	Ref.
1	BisImi-POP@2	10.30	44
2	TA-PDA-COP	5.65	45
3	TBIM	9.43	34
4	CSU-CPOPs-1	4.94	43
5	CalPOF-1	4.77	46
6	NDB-H	4.43	47
7	IHEP-51	1.561	37
8	Cu^0-MOF-303	0.837	48
9	Zn-ABTC	2.02	49
10	UiO-66-NH_2 @WCA	0.704	50
11	CityU-1	3.0	36
12	NH-COF	2.6	16
13	OM-COF-300	3.15	51
14	AIPOP-4	4.10	23
15	AZO-POP-P	3.56	52
16	PEMA	3.19	39
17	PZ-HCP-1 : 4	3.33	53
18	P-DPDA	4.08	54
19	CMP-4	2.08	42
20	P-Am	2.83	41
21	Pyrazole@ACF	3.494	38
22	Catechin@3DCF aerogel	2.227	40
23	V2D-BBL	3.0	55
24	**PPOP**	3.52	This work

[a] To better compare the I_2 capacity, the values in some references are recalculated to be in the same unit, g g^{-1}, while 1 g g^{-1} is similar to 100 wt% or 1000 mg g^{-1}.

Table 3 Kinetic parameters for the adsorption of iodine vapor by **PPOP**

Model	Parameters	
Pseudo-first order	Q_{exp} (g g^{-1})	3.52
	$Q_{e,cal}$ (g g^{-1})	1.98
	K_1 (min^{-1})	4.55×10^{-3}
	R^2	0.96904
Pseudo-second order	$Q_{e,cal}$ (g g^{-1})	3.70
	K_2 (g g^{-1} min^{-1})	4.68×10^{-3}
	R^2	0.99890

the literature. For example, TBIM, which incorporates high-density bis-imidazole units, demonstrated an impressive I_2 adsorption capacity of 9.43 g g^{-1}, significantly surpassing that of **PPOP**.[34] This substantial disparity can be attributed to the significantly higher nitrogen content in TBIM, reaching 43.13 wt%, compared to the 7.00 wt% of nitrogen content in **PPOP**. In TBIM, the imidazole moiety provides pairs of lone electrons, imparting strong electron-donating ability to the framework and enabling efficient charge transfer to the electron-deficient iodine molecules. Furthermore, the inclusion of triazine units within the TBIM backbone enhances the polarity of the polymer network, further facilitating charge-transfer-driven iodine capture. CSU-CPOPs-1 presents a distinct strategy for achieving exceptional iodine adsorption.[43] Despite its low nitrogen content of only 3.49 wt%, this material exhibits a high iodine uptake of 4.94 g g^{-1}. This performance is primarily attributed to its rigid, cross-linked network, which affords a large S_{BET} of 1032 m^2 g^{-1} and a V_{total} of 1.11 cm^3 g^{-1}. Additionally, CSU-CPOPs-1 features a unique mulberry-like hollow nanotube morphology, providing ample space for physical adsorption and enhancing iodine diffusion and retention within the porous framework. These comparisons demonstrate that decisive roles in iodine capture are played not only by electron-rich functional groups enabling chemisorption but also by physical structural properties, including high surface area, pore volume, and morphological features.

Furthermore, the absorbed iodine can be readily separated from **PPOP** by immersing the I_2-loaded **PPOP** in organic solvents. For example, when I_2-loaded **PPOP** was immersed in ethanol, the colour of the solution immediately transitioned from colourless to dark brown (Fig. S10), indicating the potential reusability of the material. To validate this hypothesis, the reusability of **PPOP** for iodine adsorption was evaluated by soaking the I_2-loaded samples in ethanol to desorb the iodine, followed by drying the samples for subsequent adsorption recycles. The results revealed that the iodine capture efficiency decreased to 84% after the first cycle and further declined to 75% after five cycles (Fig. 2d).

This reduction in capture efficiency can be attributed to the dual adsorption mechanisms involved, physisorption and chemisorption. The I_2 species adsorbed *via* physisorption can be easily removed, whereas those bound through chemisorption are more challenging to eliminate. Consequently, during the recycling process, the chemically absorbed I_2 remains persistently bound to the material. These findings underscore the potential of **PPOP** as an efficient iodine adsorbent with notable recyclability, making it a promising candidate for practical applications in iodine capture and recovery.

Furthermore, the structural stability of **PPOP** after iodine adsorption was systematically characterized. For the recycled **PPOP** after iodine adsorption, the I_2-loaded samples were thoroughly washed by Soxhlet extraction with THF for 24 h to remove the free I_2 molecules before analysis. As shown in Fig. S11, FT-IR analysis confirmed retention of all characteristic absorption bands of **PPOP**, indicating preservation of the molecular structure. As expected, the recycled **PPOP** exhibited reduced porosity, with S_{BET} of 82 ± 20 m^2 g^{-1} and V_{total} of 0.49 ± 0.01 cm^3 g^{-1}, compared to pristine **PPOP** (Table 1 and Fig. S12). Additionally, the recycled **PPOP** predominantly retained mesoporosity, with minimal microporosity in the network (Table 1 and Fig. S13). The absence of microporosity can likely be attributed to the chemically absorbed I_2 bound to the material, as evidenced by the reduction in capture efficiency after five recycling cycles. FESEM imaging of the recycled **PPOP** demonstrated that the amorphous porous morphology was maintained after iodine capture, consistent with that of pristine **PPOP** (Fig. S14). These results confirm that the fundamental framework of **PPOP** remains largely intact after iodine capture.

3.4.2. Iodine capture in solution. In addition to vapor-phase adsorption, the adsorption capacity of **PPOP** for iodine in solutions was also examined. Upon immersion in an I_2 solution in *n*-hexane solution, the colour of the solution progressively changed from purple to colourless (Fig. S15), indicating effective iodine absorption, consistent with the I_2 vapor adsorption observations. To study the iodine adsorption kinetics, experiments were conducted over a time range from 30 min to 48 h at an initial concentration of 1000 ppm. The residual iodine concentrations in the solution were monitored *via* UV-vis spectroscopy (Fig. 3a). The adsorption profile exhibited a rapid initial rate, followed by a gradual deceleration, with equilibrium being attained at approximately 36 h and a removal efficiency of 48% (Fig. 3b). The high initial adsorption rate can be attributed to the higher iodine concentration and the ease of accessibility of iodine molecules to the binding sites on **PPOP**. As the adsorption sites became occupied, the interaction between iodine and the material became more hindered, leading to a decrease in the adsorption rate. The kinetic modelling results indicated that the pseudo-second-order

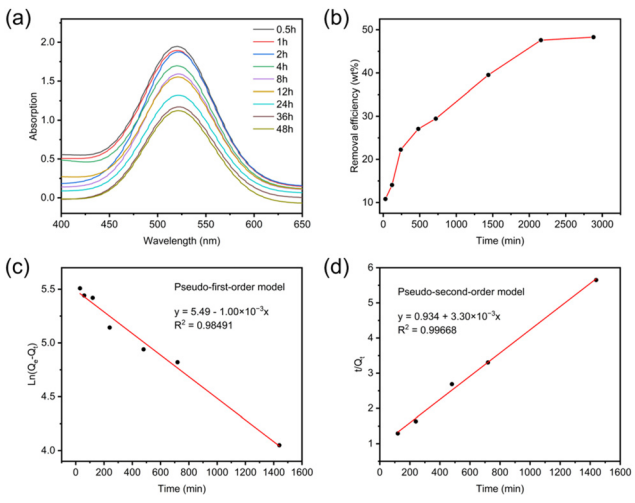

Fig. 3 (a) UV-vis adsorption spectra of the iodine solutions after being treated with **PPOP** at different time intervals; (b) effect of adsorption time on the adsorbed amount of iodine by **PPOP** suspension in *n*-hexane (1 mg mL^{-1}); (c) the pseudo-first-order model; and (d) the pseudo-second-order model.

Table 4 Kinetic parameters for the adsorption of iodine solution by **PPOP**

Model	Parameters	
Pseudo-first order	$Q_{e,\,cal}$ (mg g^{-1})	242
	K_1 (min^{-1})	1.00×10^{-3}
	R^2	0.98491
Pseudo-second order	$Q_{e,\,cal}$ (mg g^{-1})	303
	K_2 (g mg^{-1} min^{-1})	1.16×10^{-5}
	R^2	0.99668

model provided a better fit to the experimental data with an R^2 of 0.99668 (Fig. 3d and Table 4), compared to the pseudo-first-order model with an R^2 of 0.98491 (Fig. 3c and Table 4). This suggests that the iodine adsorption process on **PPOP** in hexane is predominantly controlled by chemisorption.

The adsorption isotherms of iodine solutions were studied to evaluate the interactions between iodine and **PPOP**. Fig. 4a illustrates the correlation between iodine concentrations in *n*-hexane solutions and UV absorbance, facilitating the accurate measurement of iodine concentrations in the solution. As shown in Fig. 4b, the equilibrium adsorption capacity (Q_e) of **PPOP** increased from 116 to 486 mg g^{-1} as the initial iodine concentrations (C_0) increased from 100 to 2000 ppm, ultimately attaining saturation at 486 mg g^{-1}. Furthermore, experimental data were fitted to both Langmuir and Freundlich models. The results revealed that the Freundlich model provided a superior fit (R^2 = 0.99908) compared to the Langmuir model (R^2 = 0.95237) (Fig. 4c, d, and Table S1). These results suggest that the adsorption process is primarily governed by multilayer adsorption occurring on a heterogeneous surface.[56]

3.4.3. Iodine adsorption mechanism. To elucidate the iodine adsorption mechanism, FT-IR and XPS were conducted to analyse the composition changes in the materials before and after iodine adsorption. In the FT-IR spectra, the C=N stretching vibration peaks shifted from 1614 cm^{-1} to 1533 cm^{-1} after I_2 adsorption (Fig. 5a). Simultaneously, the N–H stretching peak shifted from 3346 cm^{-1} to 3337 cm^{-1}, accompanied by a significant reduction in absorbance intensity after I_2 adsorption. These observations indicate the interactions between pyrazole units and iodine. Additionally, the C=C bands also shift from 1710 cm^{-1} to 1691 cm^{-1}, suggesting that benzene rings can also serve as binding sites for iodine capture. XPS analysis further confirmed the presence of chemical bonding between **PPOP** and iodine (Fig. S16 and 5b–c). To protect the XPS equipment, the I_2-loaded sample underwent Soxhlet extraction with ethanol for 24 h to remove free I_2 molecules prior to measurement. After I_2 adsorption, the N 1s binding energies of the H–N and C=N groups in **PPOP** increased from 399.09 eV to 399.10 eV and from 400.45 eV to 400.50 eV, respectively (Fig. 5b). Moreover, the appearance of a new peak at 401.59 eV after I_2 loading implies the formation of charge-transfer complexes (CTCs) between iodine and either the pyrazole group or the phenyl rings.[57] These binding energy shifts suggest that nitrogen atoms in the pyrazole units were positively charged due to the electrophilic reaction involving the pyrazole rings and molecular iodine (I_2), which leads to the release of iodide (I^-). The I 3d (I $3d_{3/2}$ and I $3d_{5/2}$) peaks for the I_2-loaded **PPOP** were resolved into two distinct groups: (i) 618.73 eV and 630.26 eV, and (ii) 620.47 eV and 632.02 eV (Fig. 5c). The former can be attributed to CTCs between the phenyl rings and iodine.[23] The latter is clearly due to the electrophilic reaction involving the pyrazole rings and I_2, resulting in electron transfer from the nitrogen to iodine atoms. Additionally, it is worth clarifying that while molecular iodine (I_2) can oxidize certain heterocycles, pyrazole is generally resistant to oxidation under mild conditions due to its aro-

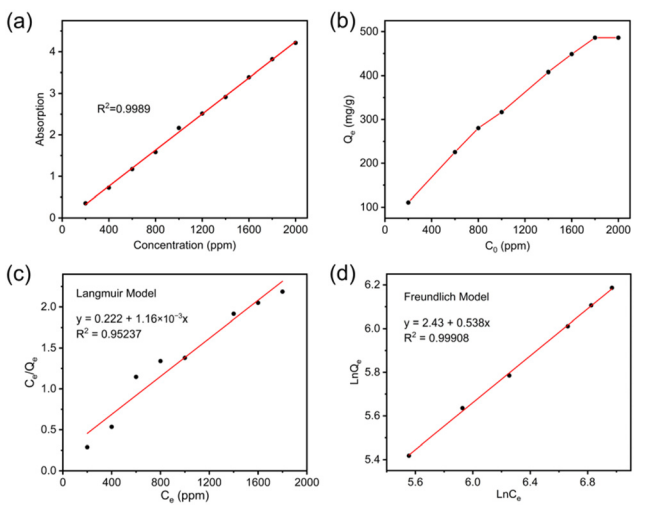

Fig. 4 (a) The fitting of the absorption value *vs.* concentration of I_2 in *n*-hexane solution with a relatively good linearity. (b) Effect of the initial iodine concentrations on the adsorption amount of iodine by **PPOP** suspension in *n*-hexane (1 mg mL^{-1}); (c) the Langmuir model; and (d) the Freundlich model.

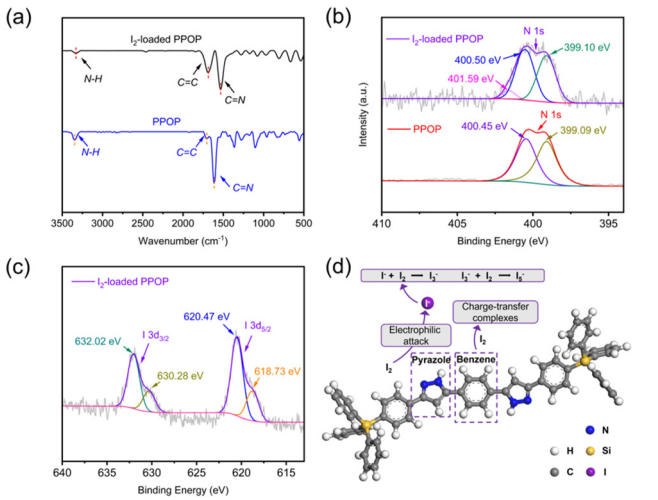

Fig. 5 (a) FT-IR spectra of pristine and iodine-loaded **PPOP**; (b) N 1s XPS spectra for pristine and iodine-loaded **PPOP**; (c) XPS spectra of I 3d for I_2-loaded **PPOP**; and (d) schematic representation of the iodine adsorption mechanism by **PPOP**.

matic stability and electron-deficient nature. However, the presence of a phenyl substituent at the pyrazole ring can increase the electron density of the system, potentially making the pyrazole ring more susceptible to electrophilic reaction with I_2. In summary, the adsorption mechanism can be described as follows. Molecular iodine (I_2) undergoes an electrophilic attack on the pyrazole units, leading to the formation of iodide (I^-). The iodide then combines with molecular iodine to form polyiodide anions (I_3^- and I_5^-). In essence, an electrophilic iodination of the pyrazole rings occurred. Apart from this pyrazole-iodine electrophilic attack process, the electron-rich phenyl rings in the framework also form CTCs with iodine.[58] In essence, this iodine adsorption is driven by electrophilic reaction or electron transfer from electron-rich units in the adsorbent to I_2, coupled with the formation of polyiodides and charge-transfer complexes (Fig. 5d), in addition to the physisorption mechanism.

3.5 Synthesis of Ag nanoparticle-loaded PPOP (PPOP-Ag) for the nitro reduction reaction

The incorporation of pyrazole units in **PPOP** offers another promising application as a support for the loading of metal ions/particles, further serving as catalysts.[59–61] To achieve this potential, silver nanoparticles (Ag NPs) loaded on **PPOP** were synthesized *via* the reduction of $AgNO_3$ using $NaBH_4$ in the presence of **PPOP** (Scheme S1). The nitrogen adsorption–desorption isotherm of PPOP-Ag revealed the S_{BET} and V_{total} of 103 ± 20 $m^2\ g^{-1}$ and 0.16 ± 0.01 $cm^3\ g^{-1}$, respectively, which are lower than those of pristine **PPOP** (Fig. S17). This reduction is attributed to the occupation of Ag NPs within the porous structure. The pore size distribution analysis of PPOP-Ag identified the presence of micropores and mesopores with average diameters at 0.78 nm, 1.41 nm, and 3.79 nm for PPOP-Ag, similar to those observed in **PPOP** (Fig. S18).

In contrast to the amorphous structure of **PPOP**, the PXRD pattern of PPOP-Ag exhibited distinct peaks at 2θ = 38.1°, 44.2°, 64.4°, and 77.5° (Fig. 6a), corresponding to the (111), (200), (220), and (311) planes of metallic silver. This result unequivocally indicated the successful incorporation of Ag NPs into the **PPOP** framework. XPS analysis confirmed the metallic state of Ag, with binding energies at 374.20 eV and 368.20 eV, corresponding to the Ag $3d_{3/2}$ and Ag $3d_{5/2}$, respectively (Fig. 6b).[62] The splitting of the 3d doublet was 6.0 eV, further substantiating the metallic state of Ag. A slight decrease of 0.08 eV in the binding energies, compared to pure Ag(0) (368.28 eV for $3d_{5/2}$ and 374.28 eV for $3d_{3/2}$), was likely attributed to interactions between Ag atoms and the nitrogen atoms in the pyrazole units of **PPOP**. Supporting this hypothesis, the N 1s binding energies of H–N and C=N exhibited positive shifts of 0.11 eV and 0.09 eV in PPOP-Ag (Fig. S19), indicating the formation of H–N–Ag and C=N–Ag interactions. ICP-AES analysis further qualified the Ag loading in PPOP-Ag at 3.08 wt%. The SEM image of PPOP-Ag revealed an amorphous structure with irregular particles (Fig. 6c). The TEM image demonstrated the uniform distribution of Ag NPs on **PPOP**, with an average size of 6.6 nm (Fig. 6d). High-resolution TEM revealed well-defined lattice fringes of the crystalline Ag NPs, with an interplanar spacing of 0.24 nm (Fig. 6e), corresponding to the (200) crystal plane of silver. Elemental mapping analysis supported the homogeneous dispersion of Ag NPs throughout the **PPOP** framework (Fig. 6f).

Subsequently, PPOP-Ag was employed as a heterogeneous catalyst for the reduction of nitroaromatics (NAs) to amine aminoaromatics (AAs), a pivotal reaction in synthetic organic chemistry[63,64] and an efficient strategy for managing toxic nitroaromatic compounds.[65] Such reductions utilizing metallic nanoparticles with $NaBH_4$ in aqueous media are well-established.[66] The typical model reaction was investigated through the reduction of 4-nitrophenol (4-NP) to 4-aminophenol (4-AP) in the presence of PPOP-Ag as the catalyst and $NaBH_4$ as the hydride source. The process was monitored using UV-vis spectroscopy. As depicted in Fig. 7a, the initial aqueous solution of 4-NP exhibits a characteristic peak at 317 nm. Upon the addition of $NaBH_4$, the absorption peak shifted to 400 nm, attributed to the formation of 4-nitrophenolate ion in alkaline solution. The

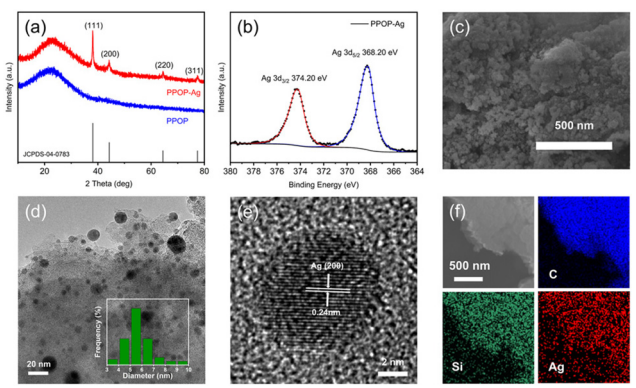

Fig. 6 (a) XRD patterns of **PPOP** and PPOP-Ag; (b) Ag 3d XPS spectra of PPOP-Ag; (c) SEM image of PPOP-Ag; (d) TEM image of PPOP-Ag (inset: histogram illustrating the particle size distribution); (e) HRTEM image of PPOP-Ag; and (f) SEM image and energy-dispersive X-ray spectroscopy elemental mappings of PPOP-Ag.

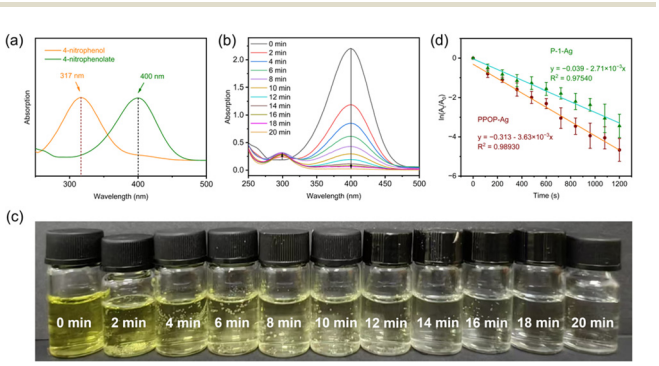

Fig. 7 (a) UV-vis spectra of 4-NP; (b) UV-vis spectra of 4-NP reduction by PPOP-Ag in deionized water from 0 min to 20 min; (c) photographs of 4-NP reduction by PPOP-Ag in deionized water from 0 min to 20 min; and (d) kinetic analysis of 4-NP reduction by PPOP-Ag and P-1-Ag.

maximum absorption at 400 nm remained unchanged over time, even after the addition of excessive $NaBH_4$ solution. In contrast, the introduction of PPOP-Ag resulted in a gradual decrease in the peak at 400 nm, accompanied by the emergence and enhancement of a peak at 300 nm, which corresponds to the formation of 4-AP. This conversion was completed within 20 min at room temperature (Fig. 7b). Furthermore, the colour of the solution changed from bright yellow to colourless, providing a visual confirmation of the reduction process (Fig. 7c).

This reduction system was also applied to other NAs. As shown in Table 5, PPOP-Ag also demonstrated catalytic activity for the reduction of various NAs. The reaction progress for all cases was monitored by UV-vis spectroscopy (Fig. S20–23), and the structures of the final products were confirmed by ^{1}H NMR spectroscopy (Fig. S24–28). As summarized in Table 5, PPOP-Ag achieved conversions of >95% at 20 min for 2-nitroaniline, 2-nitrophenol, 4-nitroaniline, and 4-nitrophenol, while reaching 72% for 4-chloronitrobenzene under identical conditions. This demonstrates effective reduction of nitro groups across diverse NAs.

The reaction conversion was calculated using C_t/C_0, based on the relative intensity of UV-vis absorbance (A_t/A_0) at 400 nm using the nitro reduction reaction of 4-NP to 4-AP as a representative example. Here, C_t represents the concentration of 4-NP at the reaction time t, and C_0 is the initial concentration of 4-NP. Given that the concentration of $NaBH_4$ was significantly higher than that of 4-NP, the concentration of $NaBH_4$ was considered constant throughout the reaction. Consequently, the reaction was assumed to be pseudo-first-order with respect to 4-NP concentration. As illustrated in Fig. 7d, the apparent rate constant (K_{app}) and the normalized rate constant (K') were calculated based on eqn (7) and (8), yielding values of $3.63 \pm 0.43 \times 10^{-3}$ s^{-1} and $3.63 \pm 0.43 \times 10^{-1}$ g^{-1} s^{-1}, respectively.

Table 5 Catalytic performance of PPOP-Ag for the nitro reduction reaction[a]

NAs	Products	Time (min)	Yield[b] (%)
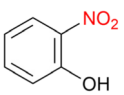	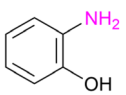	20	95
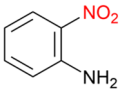	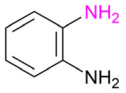	20	99
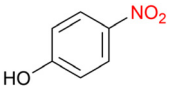	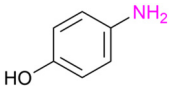	20	99
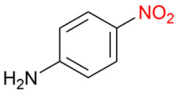	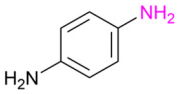	20	99
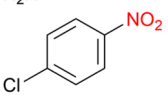	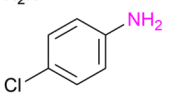	20	72

[a] Reaction conditions: PPOP-Ag (10 mg), NAs (0.1 mmol), $NaBH_4$ (1 mmol), H_2O (50 mL), r.t. [b] Isolated yield.

To assess the role of pyrazole units as anchors to the Ag NPs, **P-1** was also loaded with the Ag NPs and employed as a catalyst for the reduction of 4-NP. The results demonstrated that within 20 min, a conversion of 97% could be achieved, with K_{app} and K' of $2.73 \pm 0.34 \times 10^{-3}$ s^{-1} and $2.73 \pm 0.34 \times 10^{-1}$ g^{-1} s^{-1} (Fig. 7d). This performance was marginally inferior to that of PPOP-Ag, suggesting that the pyrazole units did not function effectively as anchoring sites for the Ag NPs.

Notably, the two catalysts exhibited distinct reusability profiles. As shown in Fig. S29, the cycling test results revealed that P-1-Ag achieved a 97% conversion in the first cycle; however, a significant decline in catalytic activity was observed in the second cycle, with the conversion dropping to merely 19%. In contrast, PPOP-Ag maintained high catalytic activity over multiple cycles, retaining a conversion of 95% even after five consecutive runs. This substantial disparity in reusability can be attributed to the different stabilities of the Ag NPs on the respective supports during the reaction. In the case of P-1-Ag, the Ag NPs were physically absorbed onto the porous framework and were prone to detachment during the reaction. Conversely, the Ag NPs loading on the porous framework of PPOP-Ag were firmly anchored due to coordination interactions with the pyrazole units. These results highlight the crucial role of the pyrazole units in **PPOP** in stabilizing the Ag NPs and ensuring consistent catalytic performance.

Additionally, to assess the structural and catalytic robustness of the catalyst, PPOP-Ag after one catalytic cycle (denoted as PPOP-Ag-1) was thoroughly characterized. FT-IR spectra showed no discernible changes compared to pristine PPOP-Ag (Fig. S30). Similar results were also observed in terms of porosity and morphology. PPOP-Ag-1 exhibited nearly identical porosity, with an S_{BET} of 104 ± 20 m^2 g^{-1} and comparable pore size distribution (Table 1 and Fig. S31–32). FESEM imaging confirmed the retention of the amorphous porous morphology (Fig. S33), closely resembling that of PPOP-Ag. Collectively, these analyses confirm the robust structural integrity of **PPOP** under catalytic conditions.

The catalytic performance of POP-Ag is comparable to that of many Ag nanoparticle-based catalysts previously reported for the reduction of 4-nitrophenol (Table 6), which underscores the potential of PPOP-Ag as an efficient catalyst for

Table 6 Comparison of the catalytic performance of PPOP-Ag with other Ag NPs based catalysts used for the reduction of 4-NP

	Ag NP-based catalysts	Apparent rate constant ($\times 10^{-3}$ s^{-1})	Ref.
1	Ag–OMS–C	30	67
2	Ag–P(ChNM)	13.1–21	68
3	SiO_2@Ag-2	9.32	69
4	Ag–TiO_2NSs	9.2	70
5	Ag–TiO_2/poly(AM-*co*-MBAM)	8.25	71
6	Ag/TP	5.27	72
7	Ag@γ-Al_2O_3	3.2	73
8	Ag NPs/C	1.69	74
9	Fe_3O_4@Ag	1.1	75
10	PPOP-Ag	3.63	This work

nitroaromatic reduction in aqueous media. However, several catalysts exhibit superior performance. For example, the Ag–OMS–C catalyst demonstrates more excellent catalytic performance than PPOP-Ag, with a higher apparent rate constant (k_{app} = 30 × 10^{-3} s^{-1}).[67] This outcome is primarily due to the Ag–OMS–C having a higher porosity (S_{BET} of 540 m^2 g^{-1} and V_{total} of 0.88 cm^3 g^{-1}) and a higher Ag loading (3.86%) compared to PPOP-Ag. These comparisons imply that the catalytic efficiency of PPOP-Ag can be further enhanced by optimizing the textural properties of the **PPOP** support. Strategies such as increasing the BET surface area and total pore volume could facilitate the dispersion of Ag nanoparticles and improve the accessibility of active sites. Additionally, increasing the overall silver loading may also contribute to a higher catalytic rate in reduction reactions.

4 Conclusions

In summary, a novel pyrazole-containing porous organic polymer (**PPOP**) has been successfully synthesized through a multicomponent tandem polymerization reaction involving tetrakis(4-ethynylphenyl)silane, terephthaloyl chloride, and hydrazine hydrate. The material demonstrates high thermal stability and good chemical stability when exposed to harsh environments. The incorporation of pyrazole units within the network imparts it with new functionalities and potential applications. **PPOP** showcases excellent iodine capturing capabilities. Specifically, it can adsorb iodine with uptakes of 3.52 ± 0.15 g g^{-1} in vapor and 486 mg g^{-1} in solution. Moreover, the material is reusable; after five adsorption–desorption cycles, its iodine capture efficiency only decreases to 75%. An in-depth analysis of the adsorption mechanism indicates that iodine capture involves a combination of physisorption and chemisorption. The chemisorption process is driven by electron transfer from electron-rich units in the adsorbent to I_2, coupled with the formation of polyiodides and charge-transfer complexes. Furthermore, **PPOP** can also act as a support for loading silver nanoparticles. The resulting material exhibits good catalytic activity for the reduction of nitroaromatics to aminoaromatics. When compared with post-synthetic modification as a viable approach for constructing pyrazole-functionalized porous polymers, the tandem polymerization strategy produces materials with enhanced structural and functional properties, including higher nitrogen content, more favorable microporosity, and enhanced iodine adsorption performance. These findings collectively suggest that **PPOP** can be efficiently employed as an efficient adsorbent for iodine capture and as a support for metal catalysts in heterogeneous catalysis. The superior iodine capture and catalytic performance attributed to the integration of pyrazole units in the porous network validates the effectiveness of functionality engineering through the multicomponent tandem polymerization. Therefore, this work may open up new avenues for the rational design and synthesis of multifunctional porous polymers and the further exploration of their applications using this straightforward strategy.

Conflicts of interest

We declare that we do not have any commercial or associative interest that represents a conflict of interest in connection with the work submitted.

Data availability

The data that support the findings of this study are available from the corresponding author, D. Wang, upon reasonable request.

Supplementary information is available. Structure characterization of monomers and polymers; UV-vis, N 1s XPS, and XRD spectra, TGA curve, and SEM image of PPOP; FT-IR spectroscopy of PPOP before and after treatment of various media; UV-vis spectra of I_2-loaded PPOP; Photographs of iodine desorption in ethanol and *n*-hexane solutions by PPOP; FT-IR spectroscopy, nitrogen adsorption and desorption isotherm, pore size distribution curve, FESEM image of the recycled PPOP sample after one cycle of iodine adsorption; Wide-scan XPS spectra of PPOP and iodine-loaded PPOP; Nitrogen adsorption and desorption isotherm, pore size distribution curve, N1s XPS spectra of PPOP-Ag; UV-vis spectra of nitroaromatics reduction by PPOP-Ag; ^{1}H NMR spectra of the reduction products; Recyclability of PPOP-Ag and P-1-Ag catalysts for 4-NP reduction in deionized water; FT-IR spectroscopy, nitrogen adsorption and desorption isotherm, pore size distribution curve, FESEM image of PPOP-Ag-1; Synthetic route of PPOP-Ag; Summary of the Langmuir and Freundlich isotherm model parameters for the adsorption of iodine solutions by PPOP. See DOI: https://doi.org/10.1039/d5lp00135h.

Acknowledgements

This research was supported by the National Natural Science Foundation of China (22271175 and 52173102).

References

1 S. Das, P. Heasman, T. Ben and S. Qiu, *Chem. Rev.*, 2017, **117**, 1515–1563.
2 J.-S. M. Lee and A. I. Cooper, *Chem. Rev.*, 2020, **120**, 2171–2214.
3 Y. Tian and G. Zhu, *Chem. Rev.*, 2020, **120**, 8934–8986.
4 K. T. Tan, S. Ghosh, Z. Wang, F. Wen, D. Rodríguez-San-Miguel, J. Feng, N. Huang, W. Wang, F. Zamora, X. Feng, A. Thomas and D. Jiang, *Nat. Rev. Methods Primers*, 2023, **3**, 1.
5 N. Chaoui, M. Trunk, R. Dawson, J. Schmidt and A. Thomas, *Chem. Soc. Rev.*, 2017, **46**, 3302–3321.

6 P. Wang, Q. Xu, Z. Li, W. Jiang, Q. Jiang and D. Jiang, *Adv. Mater.*, 2018, **30**, 1801991.
7 Z. Li and Y. Yang, *Adv. Mater.*, 2022, **34**, 2107401.
8 D.-H. Yang, Y. Tao, X. Ding and B.-H. Han, *Chem. Soc. Rev.*, 2022, **51**, 761–791.
9 X. Liu, C.-F. Liu, S. Xu, T. Cheng, S. Wang, W.-Y. Lai and W. Huang, *Chem. Soc. Rev.*, 2022, **51**, 3181–3225.
10 K. S. Song, P. W. Fritz and A. Coskun, *Chem. Soc. Rev.*, 2022, **51**, 9831–9852.
11 J. Yu, Y. Zheng, B. Lv, A. Huang, J. Zhang, Z. Wang, Y. Zhang, Y. Wu, Y. Zhou, Y. Wang and W. Luo, *Appl.Catal. B: Environ. Energy*, 2025, **368**, 125131.
12 C. Qian, W. Zhou, J. Qiao, D. Wang, X. Li, W. L. Teo, X. Shi, H. Wu, J. Di, H. Wang, G. Liu, L. Gu, J. Liu, L. Feng, Y. Liu, S. Y. Quek, K. P. Loh and Y. Zhao, *J. Am. Chem. Soc.*, 2020, **142**, 18138–18149.
13 P. Das, G. Chakraborty, N. Friese, J. Roeser, C. Prinz, F. Emmerling, J. Schmidt and A. Thomas, *J. Am. Chem. Soc.*, 2024, **146**, 17131–17139.
14 K.-H. Xie, G.-B. Wang, F. Huang, F. Zhao, J.-L. Kan, Z.-Z. Chen, L. Cai, S.-L. Han, Y. Geng and Y.-B. Dong, *Nat. Commun.*, 2025, **16**, 3493.
15 X. Wu, Y. Hong, B. Xu, Y. Nishiyama, W. Jiang, J. Zhu, G. Zhang, S. Kitagawa and S. Horike, *J. Am. Chem. Soc.*, 2020, **142**, 14357–14364.
16 N. Mokhtari and M. Dinari, *Sep. Purif. Technol.*, 2022, **301**, 121948.
17 A. Giri, Y. Khakre, G. Shreeraj, T. K. Dutta, S. Kundu and A. Patra, *J. Mater. Chem. A*, 2022, **10**, 17077–17121.
18 H. Deng, R. Hu, E. Zhao, C. Y. K. Chan, J. W. Y. Lam and B. Z. Tang, *Macromolecules*, 2014, **47**, 4920–4929.
19 B. Wei, W. Li, Z. Zhao, A. Qin, R. Hu and B. Z. Tang, *J. Am. Chem. Soc.*, 2017, **139**, 5075–5084.
20 X. Tang, C. Zheng, Y. Chen, Z. Zhao, A. Qin, R. Hu and B. Z. Tang, *Macromolecules*, 2016, **49**, 9291–9300.
21 D. Liu, H. Zhang, L. Zhang, J. Wang, Z. Chang and H. Cong, *Polym. Chem.*, 2024, **15**, 2408–2415.
22 Z.-C. Zhang, P.-L. Wang, Y.-F. Sun, T. Yang, S.-Y. Ding and W. Wang, *J. Am. Chem. Soc.*, 2024, **146**, 4822–4829.
23 B. Zhou, Z. Chen, S. Feng, D. Wang and H. Liu, *Macromolecules*, 2021, **54**, 7642–7652.
24 S. Liu, J. Li, A. Wang, D. K. P. Ng and N. Zheng, *Angew. Chem., Int. Ed.*, 2025, **64**, e202422362.
25 Y. Xia, C. Zhang and X. Zhang, *Acc. Chem. Res.*, 2025, **58**, 1345–1353.
26 A. C. Uptmoor, F. L. Geyer, F. Rominger, J. Freudenberg and U. H. F. Bunz, *ChemPlusChem*, 2018, **83**, 448–454.
27 A. Katrib, N. R. El-Rayyes and F. M. Al-Kharafi, *J. Electron Spectrosc. Relat. Phenom.*, 1983, **31**, 317–321.
28 J. Y. Lee, N. Y. Kim, D. Y. Shin, H.-Y. Park, S.-S. Lee, S. J. Kwon, D.-H. Lim, K. W. Bong, J. G. Son and J. Y. Kim, *J. Nanopart. Res.*, 2017, **19**, 98.
29 Z. Yan, Y. Yuan, Y. Tian, D. Zhang and G. Zhu, *Angew. Chem., Int. Ed.*, 2015, **54**, 12733–12737.
30 W. Xie, D. Cui, S.-R. Zhang, Y.-H. Xu and D.-L. Jiang, *Mater. Horiz.*, 2019, **6**, 1571–1595.
31 A. Sen, S. Sharma, S. Dutta, M. M. Shirolkar, G. K. Dam, S. Let and S. K. Ghosh, *ACS Appl. Mater. Interfaces*, 2021, **13**, 34188–34196.
32 J. Chang, H. Li, J. Zhao, X. Guan, C. Li, G. Yu, V. Valtchev, Y. Yan, S. Qiu and Q. Fang, *Chem. Sci.*, 2021, **12**, 8452–8457.
33 Y. Liao, J. Weber, B. M. Mills, Z. Ren and C. F. J. Faul, *Macromolecules*, 2016, **49**, 6322–6333.
34 T. Geng, C. Zhang, M. Liu, C. Hu and G. Chen, *J. Mater. Chem. A*, 2020, **8**, 2820–2826.
35 G. Shreeraj, A. Sah, S. Sarkar, A. Giri, A. Sahoo and A. Patra, *Langmuir*, 2023, **39**, 16069–16078.
36 F. Kang, X. Wang, C. Chen, C.-S. Lee, Y. Han and Q. Zhang, *J. Am. Chem. Soc.*, 2023, **145**, 15465–15472.
37 S. Deng, X. Kong, X. Fu, Z.-W. Huang, Z.-H. Zhou, L. Mei, J.-P. Yu, L.-Y. Yuan, Y.-Q. Zhu, N.-N. Wang, K.-Q. Hu and W.-Q. Shi, *Inorg. Chem.*, 2025, 224–231.
38 P. Chen, H. Zhu, T. Na, Y. Yi, J. Zhou, T. Duan and J. Lei, *Appl. Surf. Sci.*, 2024, **646**, 158917.
39 H. Tan, Y. Yang, N. Qiu, R. Tang, A. Zhou, J. Luo, X. Kong, Z. Hu, F. Zhong and P. Zhang, *Microporous Mesoporous Mater.*, 2025, **385**, 113485.
40 H. Zhu, C. Yu, B. Wang, W. Zhu, T. Duan, Y. Wei, G. He, D. Sun and J. Zhou, *Chem. Eng. J.*, 2022, **428**, 131322.
41 K. Junthod, B. Todee, K. Khamphaijun, T. Chutimasakul, T. Sangtawesin, T. Ratvijitvech, J. Tantirungrotechai, U. Suriya and T. Bunchuay, *ACS Appl. Polym. Mater.*, 2024, **6**, 7124–7136.
42 D. Dai, J. Yang, Y. Zou, J. Wu, L. Tan, Y. Wang, B. Li, T. Lu, B. Wang and Y. Yang, *Angew. Chem., Int. Ed.*, 2021, **60**, 8967–8975.
43 S. Xiong, X. Tang, C. Pan, L. Li, J. Tang and G. Yu, *ACS Appl. Mater. Interfaces*, 2019, **11**, 27335–27342.
44 T.-H. Niu, C.-C. Feng, C. Yao, W.-Y. Yang and Y.-H. Xu, *ACS Appl. Polym. Mater.*, 2021, **3**, 354–361.
45 Y. Man, X. Cui, R. Wang, S. Chai, C. Song, Y. Sun, R. Zhao and L. He, *J. Hazard. Mater.*, 2025, **490**, 137753.
46 K. Su, W. Wang, B. Li and D. Yuan, *ACS Sustainable Chem. Eng.*, 2018, **6**, 17402–17409.
47 Z. Guo, P. Sun, X. Zhang, J. Lin, T. Shi, S. Liu, A. Sun and Z. Li, *Chem. – Asian J.*, 2018, **13**, 2046–2053.
48 M. Li, X. Wang, J. Zhang, Y. Gao and W. Zhang, *Appl. Surf. Sci.*, 2023, **619**, 156819.
49 M.-M. Suo, G.-P. Yang and Y.-Y. Wang, *Cryst. Growth Des.*, 2024, **24**, 3933–3940.
50 S. Tian, Z. Yi, J. Chen and S. Fu, *J. Hazard. Mater.*, 2023, **443**, 130236.
51 T. Liu, Y. Zhao, M. Song, X. Pang, X. Shi, J. Jia, L. Chi and G. Lu, *J. Am. Chem. Soc.*, 2023, **145**, 2544–2552.
52 S. Bera, S. Sau, F. Banerjee, N. Kumar and S. K. Samanta, *Sep. Purif. Technol.*, 2025, **352**, 128123.
53 C. Yan, Y. Wu, H. Lu, H. Liu, G. Yi, M. Li, X. Cai, S. Gao and Z. Yang, *Microporous Mesoporous Mater.*, 2022, **343**, 112157.
54 J. Wang, C. Wang, H. Wang, B. Jin, P. Zhang, L. Li and S. Miao, *Microporous Mesoporous Mater.*, 2021, **310**, 110596.

55 H.-J. Noh, Y.-K. Im, S.-Y. Yu, J.-M. Seo, J. Mahmood, T. Yildirim and J.-B. Baek, *Nat. Commun.*, 2020, **11**, 2021.
56 T. Shahnaz, M. M. Fazil S, V. C. P and S. Narayanasamy, *Int. J. Biol. Macromol.*, 2020, **151**, 322–332.
57 L. He, L. Chen, X. Dong, S. Zhang, M. Zhang, X. Dai, X. Liu, P. Lin, K. Li, C. Chen, T. Pan, F. Ma, J. Chen, M. Yuan, Y. Zhang, L. Chen, R. Zhou, Y. Han, Z. Chai and S. Wang, *Chem*, 2021, **7**, 699–714.
58 A. J. A. Baskar, A. S. Rajpurohit, M. Panneerselvam, M. Jaccobb, D. RoopSingh and V. Kannappan, *Chem. Data Collect.*, 2017, **7**, 80–92.
59 D.-W. Tan, J.-B. Xie, Q. Li, H.-X. Li, J.-C. Li, H.-Y. Li and J.-P. Lang, *Dalton Trans.*, 2014, **43**, 14061–14071.
60 J. Mondal, S. K. Kundu, W. K. H. Ng, R. Singuru, P. Borah, H. Hirao, Y. Zhao and A. Bhaumik, *Chem. – Eur. J.*, 2015, **21**, 19016–19027.
61 Y. Cui, Z. Xu, H.-Y. Li, D. J. Young, Z.-G. Ren and H.-X. Li, *ACS Appl. Polym. Mater.*, 2020, **2**, 4512–4520.
62 M. Pang, J. Hu and H. C. Zeng, *J. Am. Chem. Soc.*, 2010, **132**, 10771–10785.
63 P. Zhou, L. Jiang, F. Wang, K. Deng, K. Lv and Z. Zhang, *Sci. Adv.*, 2017, **3**, e1601945.
64 D. Sokolova, T. C. Lurshay, J. S. Rowbotham, G. Stonadge, H. A. Reeve, S. E. Cleary, T. Sudmeier and K. A. Vincent, *Nat. Commun.*, 2024, **15**, 7297.
65 Q. Li, Z. Chen, H. Wang, H. Yang, T. Wen, S. Wang, B. Hu and X. Wang, *Sci. Total Environ.*, 2021, **792**, 148546.
66 K. Zhang, J. M. Suh, J.-W. Choi, H. W. Jang, M. Shokouhimehr and R. S. Varma, *ACS Omega*, 2019, **4**, 483–495.
67 H.-T. Fan, X.-G. Liu, X.-J. Xing, B. Li, K. Wang, S.-T. Chen, Z. Wu and D.-F. Qiu, *Dalton Trans.*, 2019, **48**, 2692–2700.
68 M. Arif, H. Raza, F. Tahir, S. B. Moussa, S. M. Haroon, A. Y. A. Alzahrani and T. Akhter, *J. Mol. Liq.*, 2024, **416**, 126516.
69 L. Tzounis, R. Contreras-Caceres, L. Schellkopf, D. Jehnichen, D. Fischer, C. Cai, P. Uhlmann and M. Stamm, *RSC Adv.*, 2014, **4**, 17846–17855.
70 K. Shanmugaraj, C. H. Campos, D. P. Singh, M. A. Gracia-Pinilla, J. N. D. De León, R. Aepuru and R. V. Mangalaraja, *J. Environ. Chem. Eng.*, 2024, **12**, 112588.
71 R. Sedghi, S. Asadi, B. Heidari and M. M. Heravi, *Mater. Res. Bull.*, 2017, **92**, 65–73.
72 M. Ismail, M. I. Khan, S. B. Khan, K. Akhtar, M. A. Khan and A. M. Asiri, *J. Mol. Liq.*, 2018, **268**, 87–101.
73 B. Naik, V. S. Prasad and N. N. Ghosh, *Powder Technol.*, 2012, **232**, 1–6.
74 S. Tang, S. Vongehr and X. Meng, *J. Phys. Chem. C*, 2010, **114**, 977–982.
75 G. Sharma and P. Jeevanandam, *Eur. J. Inorg. Chem.*, 2013, **2013**, 6126–6136.